



High-resolution Observations of a White-light Flare with NST

V. Yurchyshyn^{1,2}, P. Kumar², V. Abramenko^{3,4}, Y. Xu⁵, P. R. Goode¹, K.-S. Cho^{2,6}, and E.-K. Lim²

¹Big Bear Solar Observatory, New Jersey Institute of Technology, Big Bear City, CA 92314, USA

²Korea Astronomy and Space Science Institute, Daejeon, 305-348, South Korea

³Crimean Astrophysical Observatory, Nauchny, Bakhchisaray, 298409, Crimea[†]

⁴Central Astronomical Observatory of the Russian Academy of Sciences at Pulkovo, 196140, Pulkovskoye chaussee 65, Saint-Petersburg, Russia

⁵Space Weather Lab, New Jersey Institute of Technology, Newark, NJ, USA

⁶University of Science and Technology, Daejeon 305-348, South Korea

Received 2016 May 13; revised 2017 February 24; accepted 2017 February 24; published 2017 March 21

Abstract

Using high-resolution data from the New Solar Telescope, we studied fine spatial and temporal details of an M1.3 white-light (WL) flare, which was one of three homologous solar flares (C6.8, M1.3, and M2.3) observed in close proximity to the west solar limb on 2014 October 29 in NOAA active region 12192. We report that the TiO WL flare consists of compact and intense cores surrounded by less intense spatial halos. The strong and compact WL cores were measured to be ≈ 0.2 Mm across, with an area of about 10^{14} cm². Several TiO features were not cospatial with H α flare ribbons and were displaced toward the disk center by about 500 km, which suggests that the TiO and H α radiation probably did not originate in the same chromospheric volume. The observed TiO intensity enhancements are not normally distributed and are structured by the magnetic field of the penumbra.

Key words: Sun: flares – Sun: photosphere – sunspots

1. Introduction

While solar flares are well observed in the spectral lines over a wide range of electromagnetic spectra, only a few selected flares, known as white-light (WL) flares (Neidig 1989; Hudson 2016), show up in the photospheric spectral lines (e.g., Abramenko & Baranovsky 2004; Babin et al. 2016) and the visible continuum. For these flares the WL and hard X-ray (HXR) emissions were found to be spatially and temporally well correlated (Rust & Hegwer 1975; Hudson et al. 1992; Neidig & Kane 1993; Xu et al. 2004; Chen & Ding 2005; Xu et al. 2006; Fletcher et al. 2007; Wang 2009; Watanabe et al. 2010; Krucker et al. 2011), suggesting that the observed WL enhancements are linked to the flare electron precipitation sites. For a long time the WL emission was thought to be associated only with the strongest X-ray flares since it was believed that only these are capable of depositing the necessary amount of energy deep enough in the solar atmosphere to increase the intensity of the Balmer and Paschen continua. This allowed Machado et al. (1989) to classify them as type I WL flares. In type II WL flares the continuum enhancement (CE) is not accompanied by the Balmer jump and the chromospheric line enhancement is much weaker, which led Ding et al. (1999) to suggest that type II WL flares may be the result of direct energy release in the photosphere or temperature minimum region (TMR).

As the temporal and spatial resolution of solar instrumentation has improved, the “big flare” syndrome has been questioned by detection of WL emission in weak C-class flares (Matthews et al. 2003; Hudson et al. 2006; Jess et al. 2008; Kowalski et al. 2015), which lent observational support to an early suggestion by Neidig (1989) that “optical continuum is probably present in all flares” (see also Metcalf et al. 2003). At the same time, recent high-resolution data and studies of flares with the New Solar Telescope (NST, e.g., Kumar et al. 2015; Yurchyshyn et al. 2015; Lim et al. 2016) did not show any

convincing evidence of widespread photospheric intensity enhancements when observed using the TiO band at 7057 Å.

The main problem in explaining the WL emission is that it appears to be difficult to directly heat the photosphere to the required temperatures using energy transport mechanisms known to us. Alfvén waves were suggested as a possible mechanism for local acceleration of electrons in the chromosphere (Fletcher & Hudson 2008), although their efficiency was questioned (Judge et al. 2014). There is a suggestion (Fletcher & Hudson 2008; Krucker et al. 2015) that electrons may be reaccelerated in the chromosphere, which may cause them to penetrate deeper into the chromosphere. However, at this moment no evidence of such reacceleration has been observed.

The question whether electrons are able to penetrate into deep and dense layers of the solar atmosphere is currently under scrutiny. Calculations by Emslie (1978) showed that for electrons and/or protons to reach the $\tau_{5000} = 1$ level, their energy has to be of the order of a few MeV, while electron energy in the strongest flares only reaches several hundreds of keV. Considering the continuity equation for electron precipitation, Syrovatskii & Shmeleva (1972) and Dobranskii & Zharkova (2015) calculated that beam electrons with energies above 100 keV can reach the lower chromosphere with a column depth of 2×10^{21} cm⁻², while those with energies of the order of 200 keV are even capable of penetrating to the photosphere (10^{22} cm⁻²; see also Zharkova & Gordovskyy 2006). Works by other authors seem to support the idea that power-law beam electrons may precipitate throughout the entire flaring atmosphere down to the photosphere (Brown 1971; Syrovatskii & Shmeleva 1972), causing its heating via inelastic collisions with the ambient plasma via a hydrodynamic response (Somov et al. 1981; Nagai & Emslie 1984; Fisher et al. 1985; Zharkova & Zharkov 2007). These power-law electrons also cause nonthermal excitation and ionization of hydrogen and other elements, combined with radiative transfer, leading to occurrence of emission in the lines and continua during flaring events (Abouadarham & Henoux 1986; Zharkova & Kobylinskii 1993). Observations indicate that CE may be a combination of radiation that originates (i) in an optically thin

[†] While the AAS journals adhere to and respect UN resolutions regarding the designations of territories (available at <http://www.un.org/press/en>), it is our policy to use the affiliations provided by our authors on published articles.

chromospheric layer owing to heating caused by beam electrons (thermal model), with subsequent recombination producing enhanced Balmer and Paschen continuum, and (ii) in the photosphere and TMR, where the plasmas are excited and ionized directly by collisions with high-energy electrons, resulting in radiative transfer processes in spectral lines and continua, combined with backwarming radiation supplied by the heated chromosphere and corona (e.g., Hudson 1972; Metcalf et al. 1990; Babin et al. 2016; Kleint et al. 2016). Indeed, since the early 1980s the enhanced Balmer continuum has been observed close to the Balmer cutoff at 3646 Å (Neidig 1989; Kerr & Fletcher 2014), and more recently a strong increase of Balmer continuum has been detected over a wide spectral range using IRIS data (Heinzel & Kleint 2014; Kleint et al. 2016).

Accurate knowledge of the height at which continuum emission is formed may help us better understand the origin of WL flares, and several works have already addressed this question, although the findings are not always conclusive. Direct measurements of the height difference are not possible when a WL flare occurs on the solar disk. Measuring the size of WL cores as they appear in the G-band, green continuum and the near-infrared 1.56 μm line, Xu et al. (2012) indirectly estimated that the corresponding emission has originated at different heights ranging from nearly 130 km below the photosphere (1.56 μm) to 300 km above (G band). This led authors to conclude that the observations favor direct heating models since the deeper cores were smaller, which is, according to the authors, only attainable as a result of electron bombardment in a converging flux tube. Martínez Oliveros et al. (2012) measured the displacement due to the projection effect between HXR and WL sources located near the limb and found that the two were separated and located at 305 and 200 km above the photosphere, respectively. Krucker et al. (2015) studied three limb flares and directly measured that *RHESSI* HXR and *Solar Dynamics Observatory* (*SDO*)/HMI WL emissions were cospatial and originated at heights of around 800 km above the photosphere, noting that the radial extent of the WL sources ranged between 600 and 800 km. Fletcher et al. (2007) could not reliably detect any systematic offset between the HXR and WL sources. Based on the energy budget analysis, these authors concluded that CE in those events may have originated at a moderate depth of the chromosphere. Hence, the questions about the origin of WL emission in flares, the energy sources of this emission, its location and timing with respect to any other line, and continuous emission still remain wide open and need further investigation, which is the purpose of the present study.

Here we present observations of three homologous flares with WL emission of different intensity and study in detail the temporal and spatial structure of WL emission in an M1.3-class flare that occurred near the west solar limb using X-ray data from *RHESSI* (Lin et al. 2002) and the *Fermi* Gamma-ray Burst Monitor (GBM; Meegan et al. 2009), UV images acquired by the Atmospheric Image Assembly (AIA; Lemen et al. 2012) on board the *SDO* (Pesnell et al. 2012), and high-resolution images from the NST (Goode et al. 2010) and *Hinode* (Kosugi et al. 2007).

2. Data

On 2014 October 29 we observed three consecutive flares that occurred nearly every 2 hr in NOAA AR 12192 very close to the west limb at S13W77. The first C6.8 and the second

M1.3 flare from the series were observed with the NST in great detail, while the third M2.3 flare was recorded under poor seeing conditions. The NST observations were performed in the photospheric titanium oxide (TiO) band and at the chromospheric H α spectral line using the Visible Imaging Spectrometer (VIS; Cao et al. 2010). The photospheric data were acquired every 30 s using a 10 Å bandpass TiO filter centered at 7057 Å with a pixel scale of 0".0375. This absorption line (the head of the TiO γ -system) is only formed at temperatures below 4000 K, i.e., inside sunspots (see Figure 10 in Berdyugina et al. 2003). The VIS combines a 5 Å interference filter with a Fabry–Pérot etalon to produce a bandpass of 0.07 Å over a round, 70"-wide field of view (FOV). The imaging of the chromosphere was performed at five positions along the H α spectral line with a 0.4 Å step along the spectrum and a pixel size of 0".029. The difference in the acquisition time at two sequential line positions (e.g., +0.8 and -0.8 Å) was about 2 s. The five-point line scan was recorded every 30 s along the following sequence: -0.8, +0.8, -0.4, +0.4, and 0.0 Å. At each line position we obtained a speckled image with the exposure times ranging from 7 ms (at -0.8 Å) to 25 ms (at the line center). All images were acquired with the aid of an adaptive optics system, which incorporates a 357-actuator deformable mirror, a Shack–Hartmann wavefront sensor with 308 subapertures, and a digital signal processor system (Zhang et al. 2014). All collected data were speckle reconstructed with the Kiepenheuer-Institut für Sonnenphysik’s software package (KISIP; Wöger & von der Lühe 2007) to achieve the diffraction limit of the telescope over a large FOV.

The *RHESSI* images for the three flares were reconstructed by using the “CLEAN” algorithm (Hurford et al. 2002) with an integration time of 20 s, spatial resolution of 4".5, and using operational detectors #1, 3, 6, 9 and attenuator A1. While the first C6.8 and the second M1.3 flares were fully observed by *RHESSI*, it missed the impulsive phase of the third M2.3 flare and covered only its decay phase starting at 21:22:22 UT. The co-alignment between *RHESSI* and AIA data was performed as suggested by Battaglia & Kontar (2011) and Kuhar et al. (2016). *RHESSI* disk center coordinates are known with an accuracy of $>0".2$. We used *aia_prep.pro* to register and correct the AIA data. According to Battaglia & Kontar (2012), the co-alignment uncertainty between *RHESSI* and AIA data measured in the radial direction is less than 0".6, while the 90% *RHESSI* peak intensity contour in our case measures 2" across. In addition to the standard data correction, we applied the 0".15 correction suggested by Kuhar et al. (2016). For the third M2.3 flare the *Fermi* GBM (Meegan et al. 2009) X-ray data were used. To avoid pileup problems, the *Fermi* spectra were generated from the NaI 03 detector that was not the most sunward and had a cosine angle to the Sun greater than 0.5. The iodine K edge at 33.17 keV, above which an incident photon results in the release of an X-ray from K-shell transitions, is seen as a discontinuity in the response of the NaI detectors. The AIA instrument acquires full-disk EUV images of the Sun (FOV $\sim 1.3 R_{\odot}$) with a spatial resolution of 1".2 (0".6 per pixel) and a cadence of 12 s. In this study, we used 94 Å (Fe XVIII, $T \approx 6.3$ MK) and 1700 Å (continuum, $T \approx 10^4$ K) images. *Hinode* SOT (Kosugi et al. 2007; Suematsu et al. 2008; Tsuneta et al. 2008) data utilized here consist of Ca II H- and G-band images with a pixel size of 0".11.

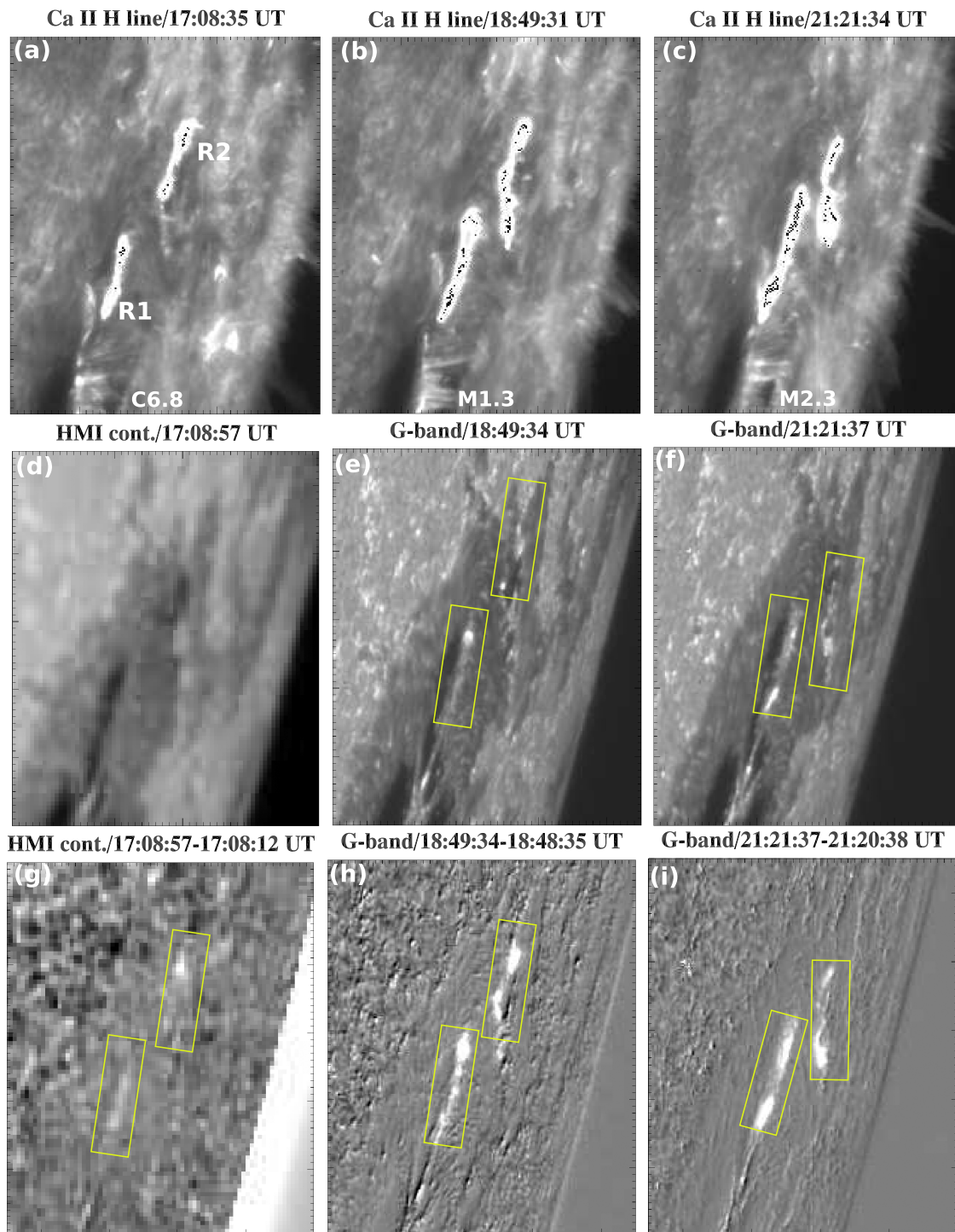


Figure 1. *Hinode* SOT Ca II H (top) and HMI and G-band intensity (middle) and their difference (bottom) images for the three flares C6.8, M1.3, and M2.3 observed on 2014 October 29 in NOAA AR 12192. HMI intensity and difference images (panels (d) and (g)) show weak WL emission during the first C6.8 flare. Each division on the x - and y -axis is equal to $1''$. R1 and R2 mark two ribbons. The yellow rectangular boxes enclose the areas with WL emission.

3. Results

The three consecutive flares of X-ray class C6.8, M1.3, and M2.3 shown in Figure 1 can be described as impulsive and confined short-duration two-ribbon flares (~ 4 – 5 minutes) with no plasma ejection and no detectable ribbon separation. Generally, a two-ribbon flare is considered to be an eruptive event accompanied with ejection of plasmas and magnetic fields (Priest 2014, p. 576). All flare ribbons were located in the

sunspot penumbra and were running along the umbra–penumbra boundary. This is particularly true for the eastern, disk-side ribbon. All flares displayed similar chromospheric features (see *Hinode* Ca II images in the top panels of Figure 1), as they repeatedly occurred in the same magnetic environment of the active region. Nevertheless, their X-ray intensities and their footprints in the photosphere were quite different. While all three flares were detected in HMI intensity (HMI.I_c) images, only the second M1.3 and the third M2.3 flares

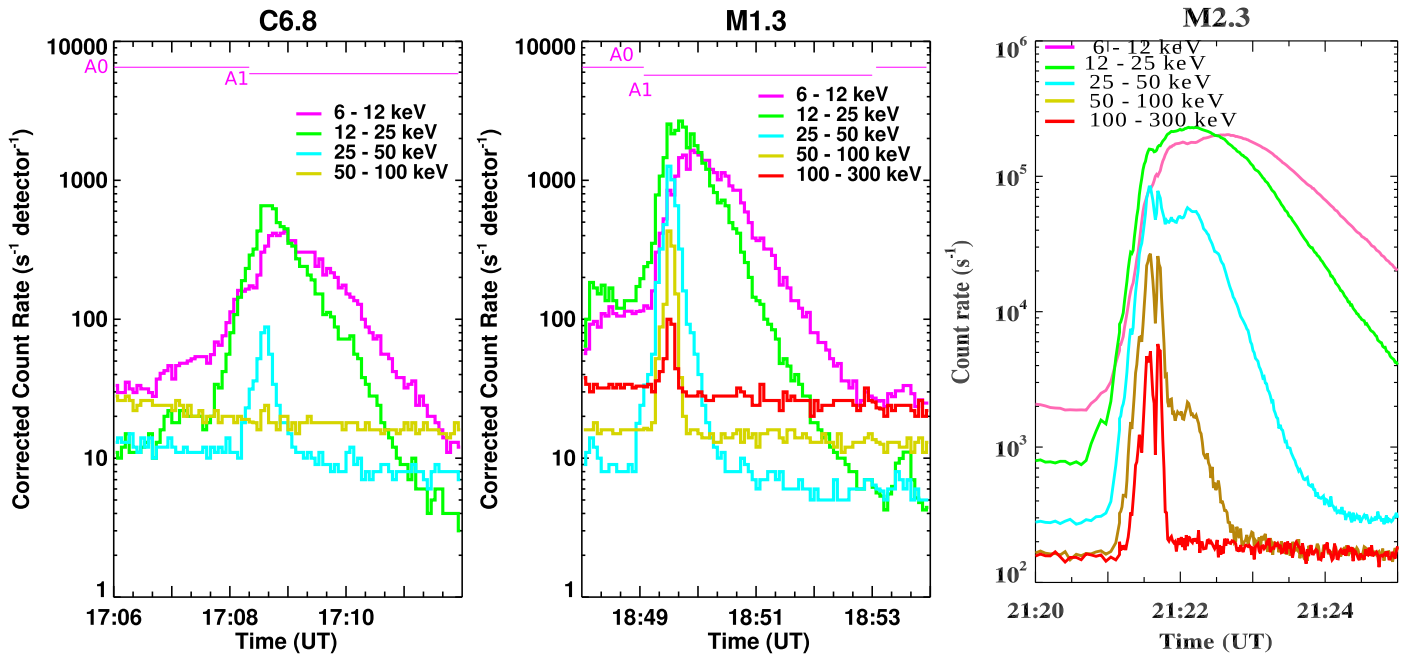


Figure 2. Left and middle panels: *RHESSI* flux profiles for the C6.8 and M1.3 flares. Horizontal A0 and A1 lines indicate the attenuator state. Right: *Fermi* GBM flux profiles for the third M2.3 flare.

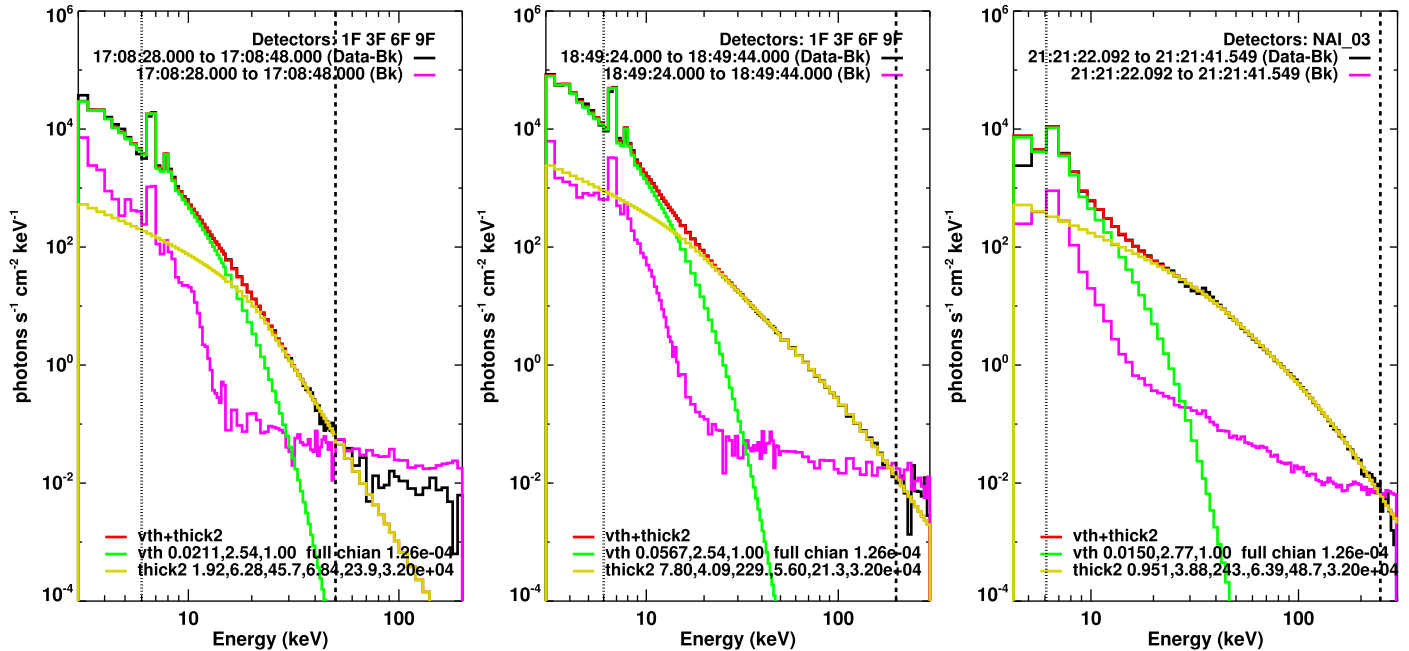


Figure 3. *RHESSI* (left and middle) and *Fermi* GBM (right) energy spectra for the three WL flares. Fitting parameters for all three events are listed in Table 1. Vertical dashed lines in each spectrum indicate the energy ranges used for fitting.

produced numerous compact NST/TiO brightenings. These two flares were also prominent in the *Hinode* SOT G-band data (middle and right panels). G-band images were not available during the impulsive phase (17:08:30–17:08:55 UT) of the first C6.8 flare, so we used HMI.I_c data instead (left panel). As evident from panels (d) and (g), the C6.8 flare CE was rather weak in the HMI.I_c image. We note that the HMI.I_c image was acquired after the C6.8 flare peak and the measured enhancement may not accurately represent the true peak flare intensity.

Figures 2 and 3 show *RHESSI* X-ray and *Fermi* GBM flux profiles and energy spectra for the three flares, which show that only M1.3 and M2.3 flares produced electrons with energies far exceeding the 50 keV level and even reaching 200 keV. The spectra fitting parameters are listed in Table 1, which shows that there is a substantial difference between spectral indices for these M-class ($\gamma = 4$) and the C-class ($\gamma = 6$) flares. We recall that the M-class flares showed TiO continuum emission, while the C6.8 flare did not. A statistical study by Battaglia et al. (2005) found no relationship between the spectral index γ and

Table 1
X-ray Spectra Fitting Parameters

Flare	T (MK)	EM (cm^{-3})	E (erg)	F_e ($e\text{ s}^{-1}$)	Index
C6.8	29.5	2.1×10^{47}	1.22×10^{29}	1.92×10^{35}	6.28
M1.3	29.5	5.6×10^{47}	2.22×10^{29}	7.80×10^{35}	4.09
M2.3	32.0	1.5×10^{47}	2.50×10^{29}	0.95×10^{35}	3.88

Note. The parameters are the temperature of the isothermal component, T ; volume emission measure, EM; thermal energy, E ; total integrated electron flux, F_e ; and the spectral index. We used *RHESSI* data for the C6.8 and M1.3 flares and *Fermi* GBM data for the M2.3 flare.

the corresponding soft X-ray flux; however, a good correspondence exists between the soft X-ray flux and the flare nonthermal flux at 35 keV.

In Figure 4 we show *RHESSI* X-ray contours overplotted on AIA 1700 Å (panels (a)–(c)) and 94 Å (panels (d)–(f)) images of the flares at their peak. For the C6.8 flare there is a complex high-energy source (25–50 keV; green contours) extended toward the 1700 Å ribbons. The second M1.3 flare produced high-energy electrons with the 50–100 keV centroids (blue contours) projected right above the AIA 1700 and 94 Å ribbons (compare panels (b), (e), and (h)). Similarly to the C6.8 flare, the disk-side HXR source is notably stronger than the limbward one and is seen to be nearly cospatial with one of the AIA 94 Å bright patches (panels (e) and (h)). *RHESSI* missed the impulsive phase of the third M2.3 flare; the existing HXR flare image data between 21:22:28 and 21:22:48 UT only show a single X-ray source with energies ranging from 6 to 50 keV.

Since the C6.8 flare did not show any CE that could be reliably detected in NST images, and the third-flare data were not usable owing to poor seeing, we only analyzed the spatial and temporal structure of TiO emission associated with the second M1.3 18:47 UT flare. In Figure 5 we plot *RHESSI* hard and soft X-ray contours over the 18:49:44 UT TiO original image and 18:49:44–18:49:14 UT difference images taken at the flare peak. The TiO image was co-aligned with a cotemporal HMI.I_c image corrected for a $0^\circ 15'$ roll as discussed in Kuhar et al. (2016). Before the roll angle correction, the peak of *RHESSI* emission was shifted relative to the HMI.I_c image by about $2''$ north, while the $0^\circ 15'$ roll caused the *RHESSI* source to become centered at the cluster of well-resolved TiO patches represented by features 2a and 2b. We thus estimate that the accuracy of *RHESSI*-TiO co-alignment is about $1''$, which is quite satisfactory for our purposes. Further in the text we will focus our attention on these TiO patches, which are also shown in Figure 6. Panel (a) is a TiO image, and panel (b) is the corresponding TiO difference image (18:47:44–18:47:14 UT). The green contours shown in all four panels outline areas with 6%, 10%, and 22% intensity increase expressed as a fraction of the averaged quiet-Sun (QS) intensity ($I_{\text{QS}} = 4160$ DN, i.e., at $\Delta I = 250, 420,$ and 900 DN). The QS intensity was derived by averaging over an area close to the sunspot. The temporal and spatial structure of these enhancements will be discussed further in the text based on Figures 6 and 7. The yellow contours outline AIA 94 Å emission excess determined by subtracting the AIA 18:49:03 UT image from the AIA 18:49:37 UT image. We estimate that the AIA and TiO data are co-aligned within $0'' 6$ accuracy, which is the pixel size of AIA data. The TiO patches 2a and 2b are cospatial with the AIA 94 Å bright feature at ($915'', -243''$) and indicated with the only right arrow in

Figures 4(e) and (h), which is also cospatial with the *RHESSI* 50–100 keV source (blue contours in Figure 4(e)). It is worth noting the following: (i) AIA 94 Å contours tend to be cospatial with brighter $H\alpha-0.8$ Å areas, and (ii) intense TiO source 1 was not associated with any AIA 94 Å emission, and the intensity of the $H\alpha-0.8$ Å ribbon at that location was much weaker than at sources 2a and 2b.

The 6% TiO contours outline patchy areas that surround very compact (<0.2 Mm across) bright cores (see boxes 1, 2a, 2b, and 3 in panel (a)). The comparison between the TiO image and the 6% contours also reveals that the latter tend to be cospatial with bright penumbral filaments and grains. We argue that the brightness excess is real and is not due to data noise. Our first argument is that the photospheric enhancements form extended patches, whereas intensity fluctuations due to instrumental, seeing, and speckle reconstruction effects would be small scale, magnetic structure independent, and highly variable in time. While most of the TiO WL features (e.g., 1, 2a, and 2b) overlap with the chromospheric flare, some are well outside the ribbons (e.g., boxes 3 and 4). We note that because the sunspot was very close to the limb, the observed E–W width of the ribbon is subject to the projection effect and is mainly composed of bright and vertically extended footpoints of the flaring loops. Because of the unrelated-to-the-flare jetting activity occurring in the foreground during the observations, the south (lower) part of the $H\alpha+0.8$ Å flare ribbon, where grains 1, 3, and 4 are located, was obscured by the jets and does not appear bright (panel (d)).

The second argument is that the TiO light curves calculated as an average intensity within the five boxes (Figure 7, green profiles) show very good agreement with the HXR, *GOES* X-ray, $H\alpha$, *Hinode* G-band, and HMI.I_c light curves. The $H\alpha$, *Hinode* G-band, and HMI.I_c light curves were normalized by the preflare intensity, which was determined by averaging 16 light-curve data points during a time interval preceding that shown in Figure 7. The TiO curves were normalized by an averaged QS intensity measured close to the sunspot.

All these instruments detected an intensity increase associated with the flare; however, the magnitude and the peak time are different. The lowest CE of about 5% was detected in HMI.I_c data, which can be at least partially attributed to spatial averaging and low spatial and temporal resolution. The combined *Hinode* G-band time profile for sources 2a and 2b showed a nearly 100% increase right at the *RHESSI* HXR peak time, while the NST/TiO intensity increased by about 25%. Sources 1, 2a, 2b, and 3 were selected because they are the brightest TiO features, while sources 3 and 4 represent low-strength enhancements outside the chromospheric flare ribbon. There are three types of time profiles in the plot. The profiles for sources 1 (dots) and 2b (dashed) (Figure 7) are similar and feature a sharp 1-minute-wide peak followed by a nearly 3-minute-long plateau that ended at 18:53:30 UT. These profiles are reminiscent of those reported by Xu et al. (2006), and they are thought to manifest the occurrence of a strong impulsive heating event followed by a cooling period. These peaks appear to be slightly delayed relative to the HXR peak (vertical dashed line), mainly due to the insufficient temporal resolution. The thick green line (low-intensity enhancement at source 4) is similar to source 1 and 2b profiles, with one exception: it does not feature a peak as well defined as these other two. Finally, the open circle line represents intensity variations at source 3, which was bright and situated outside the flare ribbon as well.

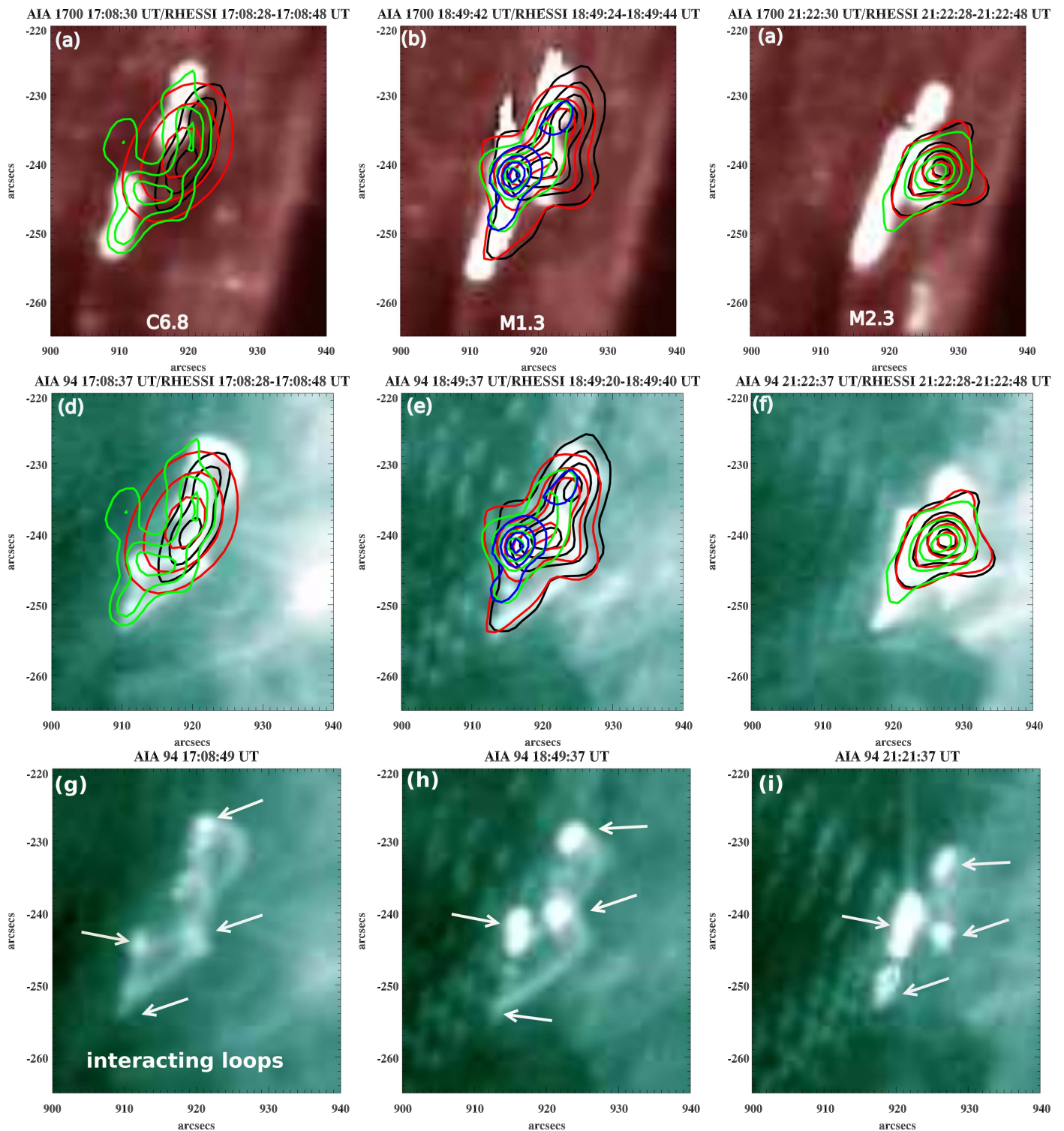


Figure 4. *RHESSI* X-ray contours (black: 6–12 keV; red: 12–25 keV; green: 2–50 keV; and blue: 50–100 keV) plotted over AIA 1700 Å (top) and 94 Å (middle and bottom) images of flares. The contour levels in the panels (b), (c), (e), and (f) are plotted at 30%, 50%, 70%, and 90% of the peak intensity. In panels (a) and (d) the contour levels are at 50%, 70%, and 90% of the peak intensity. Panels (g), (h), and (i) show the same AIA 94 Å images but without contours to emphasize the presence of bright loop footpoints, indicated by arrows, and what appears to be loops interacting during the impulsive phase of the WL flares.

This profile appears rather $H\alpha$ -like with a gradual rise and decrease. Its peak was delayed relatively to the 1, 2a, and 4 profiles and the HXR peak (dashed vertical line). The upper middle panel of Figure 2 shows that *RHESSI* 6–12 keV emission and *GOES* 0.5–4 Å flux were both similarly delayed relative to the HXR peak.

The displacement between sources 3 and 4 and the chromospheric ribbons suggests that the TiO and $H\alpha$ emission could have originated at different heights in the solar atmosphere and the displacement is due to the projection effect. The TiO kernels were displaced eastward relative to the $H\alpha$ –0.8 Å features by about 500 km ($0''.7$) when viewed near

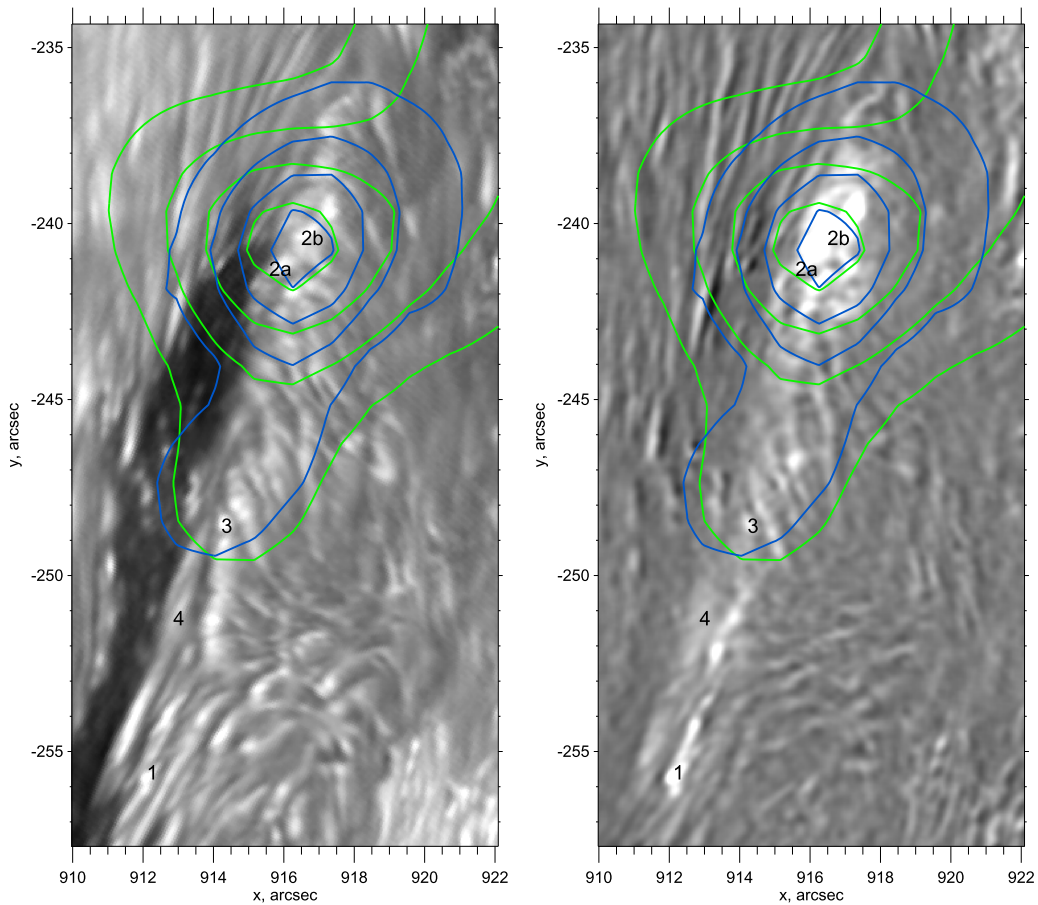


Figure 5. *RHESSI* X-ray contours (green: 25–50 keV; blue: 50–100 keV) plotted over 18:49:44 UT NST TiO (left) and TiO difference (18:49:44–18:49:14 UT) (right) images of the M1.3 flare. *RHESSI* contour levels are plotted at 30%, 50%, 70%, and 90% of the corresponding peak intensity. Numbers 1, 2a, 2b, 3, and 4 indicate TiO patches discussed in the study.

the west limb at 77° longitude. This means that the vertical offset between the two emitting volumes was about 500 km. Considering that the visible continuum observed near the solar limb is formed on average 350 km higher than that at the disk center (i.e., near the TMR; Abouharham & Henoux 1986), the lower boundary of the $H\alpha$ – 0.8 \AA emitting volume can be placed at heights of about 900 km above the $\tau_{5000} = 1$ level (as defined at the disk center), which is a quite reasonable estimate (Krucker et al. 2015).

Rapid decrease of TiO intensity from $1.1I_{QS}$ at 18:49:44 UT to $0.9I_{QS}$ at 18:50:14 UT indicates that the cooling time in the photosphere is less than 30 s (see also Xu et al. 2006). It is interesting, however, that all four TiO light curves showed a plateau in the light curves between 18:50:30 UT and 18:53:30 UT, which lasted until about 30 s after the *RHESSI* 6–25 keV flux has diminished.

In Figure 8 we plot the probability distribution function (PDF) of the TiO intensity difference. The distribution is non-Gaussian and consists of normally distributed negative differences, a strong peak at zero, and a heavy tail reaching 1400 DN, which is about 30% of QS TiO intensity. The 250 DN contour in Figure 6(b) very well outlines the TiO WL patches, suggesting that data noise does not exceed 250 DN (i.e., $<6\%$ of I_{QS}). The negative wing of the distribution is cut off at -200 DN and also represents the data noise since it is not likely that we have observed a strong flare-related darkening in the photosphere. In this case we can assume that the noise is represented in the observed distribution by a Gaussian (thin

line), which was calculated by fitting the negative part of the PDF. The shaded area is the residual after the “noise” Gaussian was subtracted from the observed PDF, and it mainly represents the distribution of the TiO enhancements at the flare pixels. That residual distribution is plotted again in the linear (x)–logarithmic (y) coordinate system in the inset of Figure 8. It exhibits a three-part structure, with a rounded peak at $I = 230$ DN, a linear interval (260–950 DN), and a nearly horizontal interval in the range above 1000 DN. The normally distributed intensities between 200 and 350 DN represent the spatial “halos” (Xu et al. 2006) around bright sources. The compact WL areas have their intensities distributed according to the exponential law with index 0.58. These brightest cores are outlined in Figure 6(b) by the 900 DN (22%) contour and represent small and concentrated intensity enhancements such as sources 1, 2a, 2b, and 3.

4. Summary and Discussion

Three homologous solar flares have been observed in a close proximity to the west solar limb. The two strongest flares, the M1.3 at 18:49 UT and the M2.3 at 21:21 UT, were associated with WL emission observed in *Hinode* G-band 4305 \AA , HMI Fe I 6173 \AA , and NST TiO 7059 \AA spectral ranges. While the weakest C6.8 flare at 17:08 UT failed to produce any detectable signature in the high-resolution NST TiO data, the HMI.L_c difference images showed a weak (several percent) CE. The fact that no TiO WL emission was detected in the C6.8

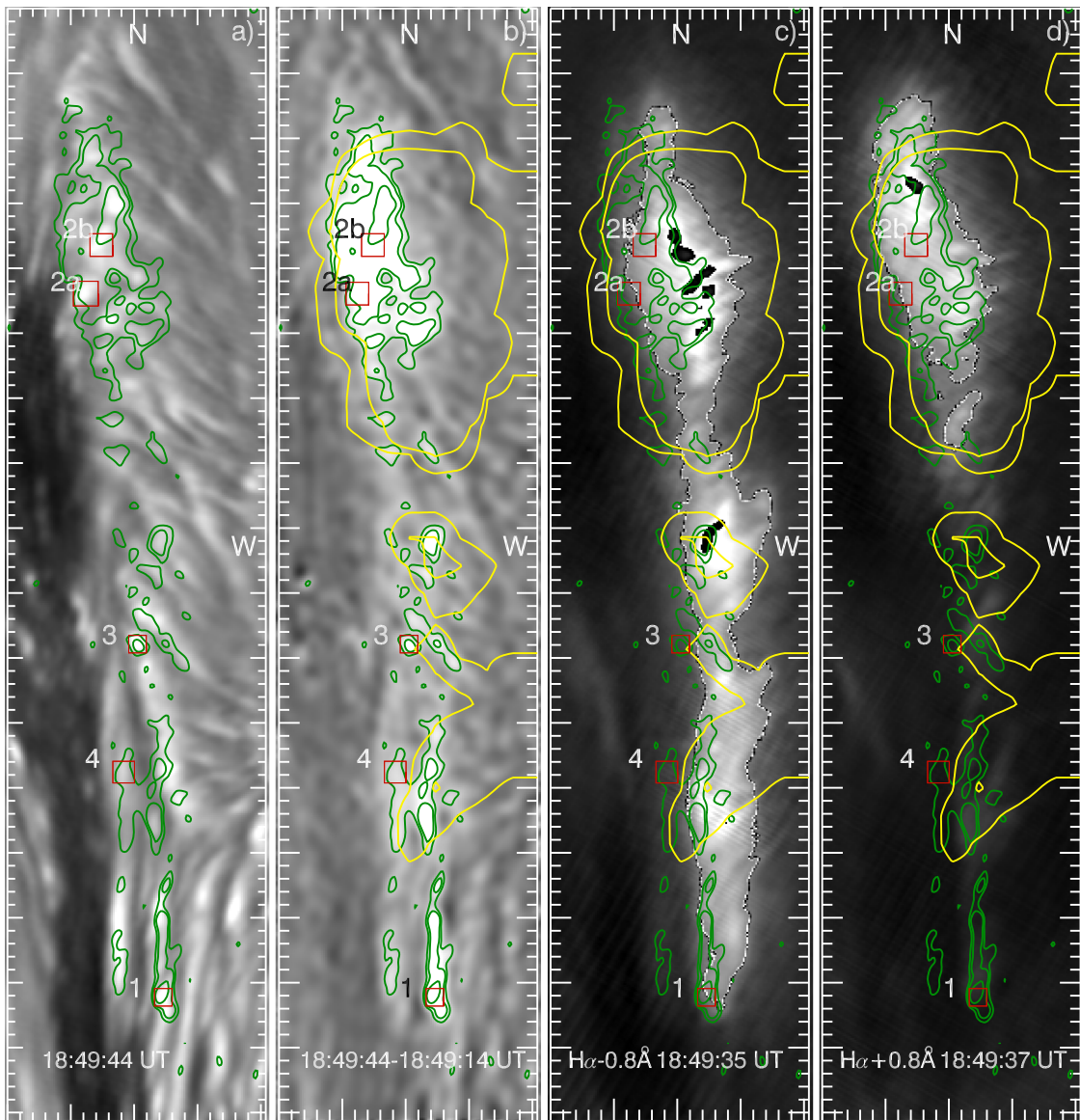


Figure 6. M1.3 WL flare as seen at the HXR peak time with TiO 7057 Å (panel (a)) and H α filters (panels (c) and (d)). Panel (b) is a TiO difference image (18:49:44–18:49:14 UT). The green contours plotted in all panels outline TiO intensity enhancements at 6%, 10%, and 22% levels of the QS intensity. The red boxes outline areas where the intensity profiles were determined. The yellow contours outline AIA 94 Å emission. The sunspot umbra can be seen at the left side of panel (a). Note that the south (lower) half of the H α +0.8 Å ribbon (panel (d)) is not seen here, as it was obscured by unrelated jets occurring in the foreground. The large tick interval is 1 Mm. The dark patches inside the flare ribbon (panels (c) and (d)) represent saturated pixels.

flare cannot simply be attributed to low spatial resolution, as suggested by Jess et al. (2008), and is most likely related to the flare energy. *RHESSI* and *Fermi* photon spectra for the M1.3 and M2.3 flares showed strongly accelerated electrons in the 50–100 keV energy range, while no electrons above 50 keV were detected in the C6.8 flare. This indicates the important role that energetic electrons might play in producing WL emission in these flares. This inference is also well aligned with the conclusion by Kuhar et al. (2016) that 50 keV flare-accelerated electrons are the main source for WL production. Analyzing 13 WL flares, Huang et al. (2016) also concluded that stronger WL emission tends to be associated with a larger population of high-energy electrons.

Intense and compact 10%–25% TiO intensity enhancements are ≈ 0.2 Mm across and occupy an area of about 10^{14} cm 2 , which is one of the lowest reported so far. Jing et al. (2016) obtained the same order-of-magnitude areas from NST/VIS

H α +1 Å images probing the lower chromosphere. The above measurements are nearly one to two orders of magnitude smaller than the previous measurements made in optical (e.g., Jess et al. 2008; Xu et al. 2012; Krucker et al. 2015) and HXR (Dennis & Pernak 2009; Kennedy et al. 2015) spectral ranges. Several TiO cores were not cospatial with the H α emission and shifted by about ~ 0.7 (500 km) toward the disk center, lying entirely outside the chromospheric ribbons. Assuming that the displacement was due to a projection effect, we find that the associated H α –0.8 Å emission originated ~ 500 km above the TiO formation level at that longitude, which argues against the idea that these strong cores observed with the TiO filter formed in an optically thin chromospheric layer from the recombination spectra. The NST has already observed several flares of various intensity, including X-class events, but the TiO flares were not observed during each and every event. While other flares were located on the disk, where the TiO band is

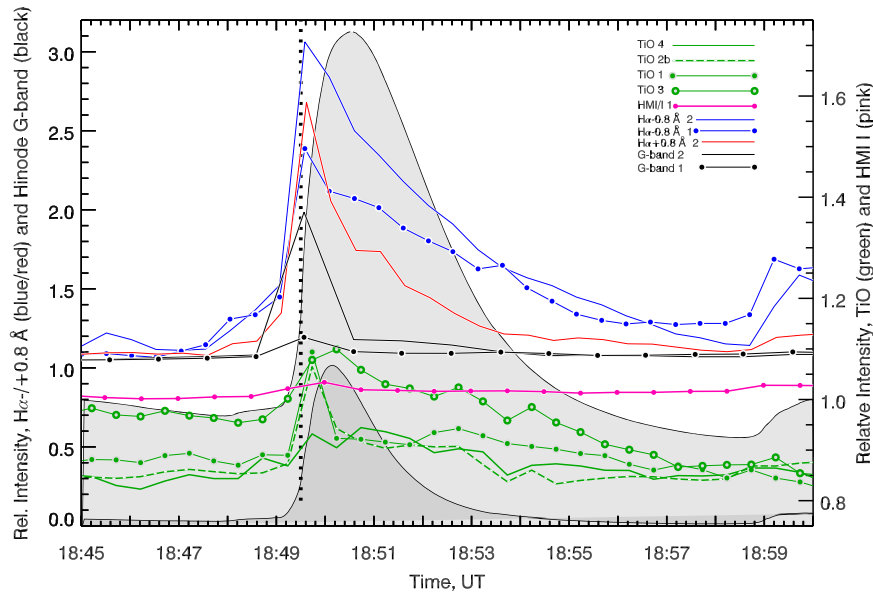


Figure 7. Light curves for the M1.3 WL flare determined from NST/TiO (green), HMI I_c (pink), *Hinode* G band (black), NST H α −0.8 Å (blue), and NST H α +0.8 Å (red) images. The light and dark shaded curves show *GOES* 1–8 Å and *GOES* 0.5–4.0 Å flux variations, respectively. The dots represent the intensity profiles for source 1 (see Figure 6). The red, blue, and black curves without symbols are time profiles for combined sources 2a and 2b, since they could not be separated in H α , *Hinode*, and HMI images. The green dashed line is for source 2b, the thick green line is for source 4, and the open circle line is for source 3. The measured intensity is the average intensity of all source pixels normalized by the preflare intensity level. The TiO light curves were normalized by the QS intensity.

thought to be formed at heights of about 150 km, the flare discussed here occurred near the limb, where the emission is expected to originate at 350 km above the $\tau_{5000} = 1$ level. This suggests that the TiO flare emission probably originates in the upper photosphere. Martínez Oliveros et al. (2012) placed the HXR and HMI 6173 Å emission at the same range of heights. We note that in a nonflaring atmosphere the HMI 6173 Å line core forms in the upper photosphere as well (200–300 km; Norton et al. 2006) (limb observations show that during flares 6173 Å emitting plasma may extend higher into the chromosphere; e.g., Krucker et al. 2015), and that may be the reason why WL flares are frequently detected in HMI I_c data (e.g., Martínez Oliveros et al. 2012; Krucker et al. 2015; Kuhar et al. 2016).

It has been reported that WL emission consists of compact cores with intensity peaks cotemporal with the HXR peaks and more extended “halos” that peak several tens of seconds later (Xu et al. 2006). The NST data allowed us to further refine the details of spatial and temporal distribution of WL emission. First, the observed TiO emission could be decomposed into three components: (i) weaker CEs (<10% of I_{QS}), which show nearly Gaussian distribution; (ii) midrange CEs (10%–20% of I_{QS}), which are distributed exponentially; and (iii) strongest intensities (>20% of I_{QS}), which are nearly independent of the amplitude. Second, both TiO cores and “halos” appear to be structured by magnetic fields, in this particular case, by the penumbral grains and filaments. Even the weakest CEs of about 6% of the QS intensity were either stretched along the bright parts of penumbral filaments or associated with penumbral grains. Finally, we distinguished three types of flare light curves: (i) HXR-like profiles with a rapid (<30 s) rise and an equally abrupt drop, followed by a \sim 3-minute-long plateau of enhanced brightness (\sim 5%–10% of I_{QS} ; the TiO and *RHESSI* HXR peaks are cotemporal); (ii) H α or soft-X-ray-like profiles with slower and gradual rise that peaked nearly simultaneously with the H α ±0.8 Å flux (a weak \sim 6% plateau is also present);

and (iii) intensity profiles without a prominent peak (plateau only).

The variety of light curves measured during the M1.3 flare suggests that more than one continuum emission mechanism may operate during a flare. Direct heating by high-energy electrons may be responsible for the compact and intense TiO cores. This suggestion is mainly based on (i) the compact size of the TiO cores, (ii) their displacement from the chromospheric flare structures, and (iii) their strict alignment with the magnetic field structures. Also, the 50–100 keV centroids in the second M1.3 flare were observed right above the AIA 1700 Å and 94 Å bright patches, which were cospatial with the TiO sources 2a and 2b. This spatial and temporal correspondence between the *RHESSI* HXR and TiO signatures is another argument for the direct heating during the M1.3 flare. The extended and weaker “halos” around the cores, as well as the TiO patches without the impulsive part (profiles 3 and 4), may be either (i) photospheric emission due to backwarming radiation (Neidig & Kane 1993) or (ii) optically thin chromospheric emission from the recombination spectra. However, the fact that these “halos” are well aligned with the photospheric penumbral structures and encircle intense cores argues against the optically thin emission mechanism. Nevertheless, these inferences are suggestive, and detailed analysis of electron energy spectra and continuum emission is needed to produce final conclusions.

Finally, two-ribbon flares are considered to be eruptive flares accompanied by ejection of plasma and magnetic fields (Priest 2014, p. 576). However, we did not observe any plasma ejection or coronal mass ejection associated with these flares, so they seem to be rare, confined two-ribbon flares similar to that observed by Cheng et al. (2015). The AIA 94 Å data revealed formation of four flare footpoints during the impulsive phase, which later formed a two-ribbon configuration. Kumar et al. (2010) detected for the first time four flare footpoints in the *GOES* X-ray images (6–65 Å channel) during the flare

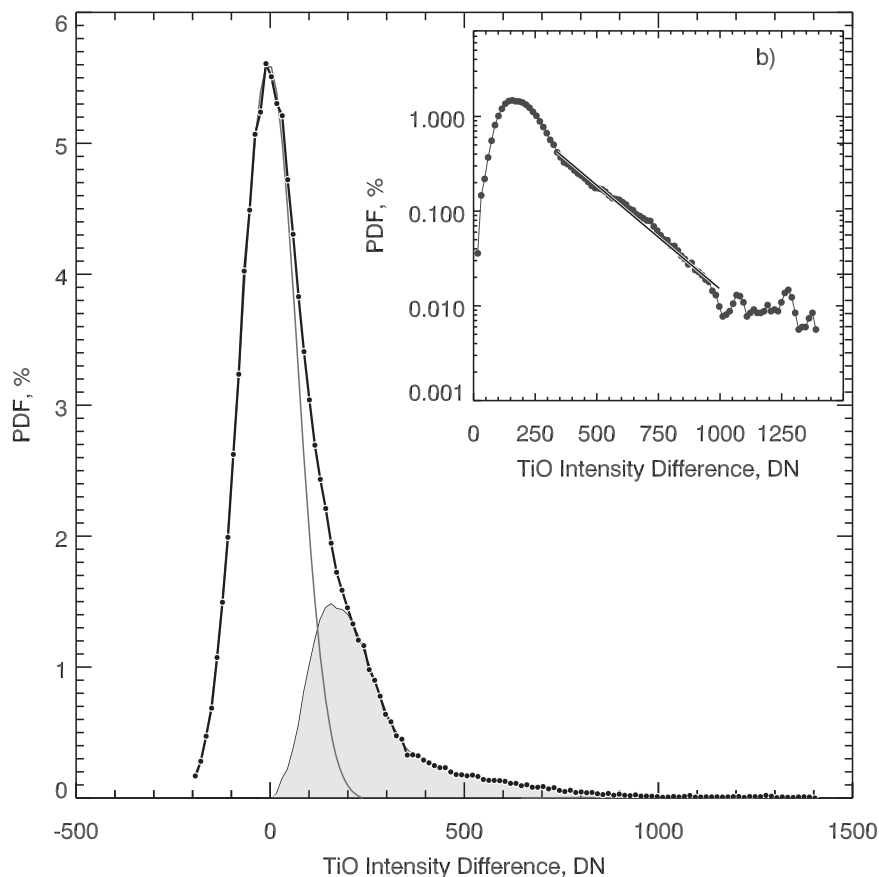


Figure 8. Measured PDF of the TiO continuum enhancements (thick dotted line). The Gaussian (thin solid curve) represents data noise in the difference image shown in Figure 6 assuming that all negative values are due to data noise. The shaded area is the residual after the noise Gaussian was subtracted from the measured PDF. This residual distribution is plotted in the inset, where the line represents a linear fit to the exponential law.

initiation that later led to the formation of a confined two-ribbon flare. That and other similar events are thought to be associated with the X-type loop–loop interaction driven by shear motions of the loop footpoints (Tajima et al. 1982; Sakai & de Jager 1996). In our case we also see evidence of loop–loop interaction in all three flares. Although we do not observe a clear X-type loop configuration, due to the compact size of the flare ribbons, the X and I type loop interaction cannot be excluded. The fact that both interacting loops were rooted at the umbra–penumbra boundary of large sunspots also indicates that strong magnetic fields were involved in the interaction, which ensures a high reconnection rate and efficient electron acceleration (e.g., Lin 2011).

We thank the referee for careful reading of the manuscript and valuable suggestions and criticism that led to significant improvement of the paper. *SDO* is a mission for NASA’s Living With a Star (LWS) program. The *SDO* data were provided by the Korean Data Center (KDC) for *SDO* in cooperation with NASA and the *SDO/HMI* team. *RHESSI* is a NASA Small Explorer. *Hinode* is a Japanese mission developed and launched by ISAS/JAXA, with NAOJ as domestic partner and NASA and STFC (UK) as international partners. BBSO operation is supported by NJIT, US NSF AGS-1250818, and NASA NNX13AG14G grants, and NST operation is partly supported by the Korea Astronomy and Space Science Institute (KASI), Seoul National University, and by the strategic priority research program of CAS with Grant no. XDB09000000. We thank Valentina Zharkova for valuable insights in the physics of

electron precipitation and Kim Tolbert for many helpful discussions on *RHESSI/Fermi* data. V.Y. acknowledges support from AFOSR FA9550-15-1-0322 and NSF AST-1614457 grants and KASI. We thank the International Space Science Institute in Bern for enabling interesting discussions. X.Y. acknowledges support from NASA NNX16AF72G and NSF AGS 1539791 grants. K.-S.C. acknowledges support from the US Air Force Research Laboratory, under agreement FA 2386-14-1-4078, and by the “Planetary System Research for Space Exploration” grant from KASI.

References

- Aboudarham, J., & Henoux, J. C. 1986, *A&A*, **156**, 73
Abramenko, V. I., & Baranovsky, E. A. 2004, *SoPh*, **220**, 81
Babin, A. N., Baranovskii, E. A., & Koval’, A. N. 2016, *ARep*, **60**, 768
Battaglia, M., Grigis, P. C., & Benz, A. O. 2005, *A&A*, **439**, 737
Battaglia, M., & Kontar, E. P. 2011, *A&A*, **533**, L2
Battaglia, M., & Kontar, E. P. 2012, *ApJ*, **760**, 142
Berdyugina, S. V., Solanki, S. K., & Frutiger, C. 2003, *A&A*, **412**, 513
Brown, J. C. 1971, *SoPh*, **18**, 489
Cao, W., Gorceix, N., Coulter, R., et al. 2010, *AN*, **331**, 636
Chen, Q. R., & Ding, M. D. 2005, *ApJ*, **618**, 537
Cheng, X., Hao, Q., Ding, M. D., et al. 2015, *ApJ*, **809**, 46
Dennis, B. R., & Pernak, R. L. 2009, *ApJ*, **698**, 2131
Ding, M. D., Fang, C., & Yun, H. S. 1999, *ApJ*, **512**, 454
Dobranskis, R. R., & Zharkova, V. V. 2015, *MNRAS*, **453**, 229
Emslie, A. G. 1978, *ApJ*, **224**, 241
Fisher, G. H., Canfield, R. C., & McClymont, A. N. 1985, *ApJ*, **289**, 414
Fletcher, L., Hannah, I. G., Hudson, H. S., & Metcalf, T. R. 2007, *ApJ*, **656**, 1187
Fletcher, L., & Hudson, H. S. 2008, *ApJ*, **675**, 1645

- Goode, P. R., Yurchyshyn, V., Cao, W., et al. 2010, *ApJL*, 714, L31
- Heinzel, P., & Kleint, L. 2014, *ApJL*, 794, L23
- Huang, N.-Y., Xu, Y., & Wang, H. 2016, *RAA*, 16, 177
- Hudson, H. S. 1972, *SoPh*, 24, 414
- Hudson, H. S. 2016, *SoPh*, 291, 1273
- Hudson, H. S., Acton, L. W., Hirayama, T., & Uchida, Y. 1992, *PASJ*, 44, L77
- Hudson, H. S., Wolfson, C. J., & Metcalf, T. R. 2006, *SoPh*, 234, 79
- Hurford, G. J., Schmahl, E. J., Schwartz, R. A., et al. 2002, *SoPh*, 210, 61
- Jess, D. B., Mathioudakis, M., Crockett, P. J., & Keenan, F. P. 2008, *ApJL*, 688, L119
- Jing, J., Xu, Y., Cao, W., et al. 2016, *NatSR*, 6, 24319
- Judge, P. G., Kleint, L., Donea, A., Sainz Dalda, A., & Fletcher, L. 2014, *ApJ*, 796, 85
- Kennedy, M. B., Milligan, R. O., Allred, J. C., Mathioudakis, M., & Keenan, F. P. 2015, *A&A*, 578, A72
- Kerr, G. S., & Fletcher, L. 2014, *ApJ*, 783, 98
- Kleint, L., Heinzel, P., Judge, P., & Krucker, S. 2016, *ApJ*, 816, 88
- Kosugi, T., Matsuzaki, K., Sakao, T., et al. 2007, *SoPh*, 243, 3
- Kowalski, A. F., Cauzzi, G., & Fletcher, L. 2015, *ApJ*, 798, 107
- Krucker, S., Hudson, H. S., Jeffrey, N. L. S., et al. 2011, *ApJ*, 739, 96
- Krucker, S., Saint-Hilaire, P., Hudson, H. S., et al. 2015, *ApJ*, 802, 19
- Kuhar, M., Krucker, S., Martínez Oliveros, J. C., et al. 2016, *ApJ*, 816, 6
- Kumar, P., Srivastava, A. K., Somov, B. V., et al. 2010, *ApJ*, 723, 1651
- Kumar, P., Yurchyshyn, V., Wang, H., & Cho, K.-S. 2015, *ApJ*, 809, 83
- Lemen, J. R., Title, A. M., Akin, D. J., et al. 2012, *SoPh*, 275, 17
- Lim, E.-K., Yurchyshyn, V., Park, S.-H., et al. 2016, *ApJ*, 817, 39
- Lin, R. P. 2011, *SSRv*, 159, 421
- Lin, R. P., Dennis, B. R., Hurford, G. J., et al. 2002, *SoPh*, 210, 3
- Machado, M. E., Emslie, A. G., & Avrett, E. H. 1989, *SoPh*, 124, 303
- Martínez Oliveros, J.-C., Hudson, H. S., Hurford, G. J., et al. 2012, *ApJL*, 753, L26
- Mathews, S. A., van Driel-Gesztelyi, L., Hudson, H. S., & Nitta, N. V. 2003, *A&A*, 409, 1107
- Meegan, C., Lichti, G., Bhat, P. N., et al. 2009, *ApJ*, 702, 791
- Metcalf, T. R., Alexander, D., Hudson, H. S., & Longcope, D. W. 2003, *ApJ*, 595, 483
- Metcalf, T. R., Canfield, R. C., & Saba, J. L. R. 1990, *ApJ*, 365, 391
- Nagai, F., & Emslie, A. G. 1984, *ApJ*, 279, 896
- Neidig, D. F. 1989, *SoPh*, 121, 261
- Neidig, D. F., & Kane, S. R. 1993, *SoPh*, 143, 201
- Norton, A. A., Graham, J. P., Ulrich, R. K., et al. 2006, *SoPh*, 239, 69
- Pesnell, W. D., Thompson, B. J., & Chamberlin, P. C. 2012, *SoPh*, 275, 3
- Priest, E. 2014, *Magnetohydrodynamics of the Sun* (2nd ed.; Cambridge: Cambridge Univ. Press)
- Rust, D. M., & Hegwer, F. 1975, *SoPh*, 40, 141
- Sakai, J.-I., & de Jager, C. 1996, *SSRv*, 77, 1
- Somov, B. V., Spektor, A. R., & Syrovatskii, S. I. 1981, *SoPh*, 73, 145
- Suematsu, Y., Tsuneta, S., Ichimoto, K., et al. 2008, *SoPh*, 249, 197
- Syrovatskii, S. I., & Shmeleva, O. P. 1972, *AZh*, 49, 334
- Tajima, T., Brunel, F., & Sakai, J. 1982, *ApJL*, 258, L45
- Tsuneta, S., Ichimoto, K., Katsukawa, Y., et al. 2008, *SoPh*, 249, 167
- Wang, H.-M. 2009, *RAA*, 9, 127
- Watanabe, K., Krucker, S., Hudson, H., et al. 2010, *ApJ*, 715, 651
- Wöger, F., & von der Lühe, O. 2007, *ApOpt*, 46, 8015
- Xu, Y., Cao, W., Jing, J., & Wang, H. 2012, *ApJL*, 750, L7
- Xu, Y., Cao, W., Liu, C., et al. 2004, *ApJL*, 607, L131
- Xu, Y., Cao, W., Liu, C., et al. 2006, *ApJ*, 641, 1210
- Yurchyshyn, V., Kumar, P., Cho, K.-S., Lim, E.-K., & Abramenko, V. I. 2015, *ApJ*, 812, 172
- Zhang, X., Gorceix, N., Schmidt, D., et al. 2014, *Proc. SPIE*, 9148, 914850
- Zharkova, V. V., & Gordovskyy, M. 2006, *ApJ*, 651, 553
- Zharkova, V. V., & Kobylinskii, V. A. 1993, *SoPh*, 143, 259
- Zharkova, V. V., & Zharkov, S. I. 2007, *ApJ*, 664, 573